

Direct wavefront sensing enables functional imaging of infragranular axons and spines

Rui Liu¹, Zengyi Li¹, Jonathan S. Marvin² and David Kleinfeld^{1,3*}

We advance two-photon microscopy for near-diffraction-limited imaging up to 850 μm below the pia in awake mice. Our approach combines direct wavefront sensing of light from a guidestar (formed by descanned fluorescence from Cy5.5-conjugated dextran in brain microvessels) with adaptive optics to compensate for tissue-induced aberrations in the wavefront. We achieve high signal-to-noise ratios in recordings of glutamate release from thalamocortical axons and calcium transients in spines of layer 5b basal dendrites during active tactile sensing.

Two-photon laser scanning microscopy is indispensable for imaging through the mammalian brain with subcellular resolution¹. However, resolution and efficiency decrease with depth as a result of scattering and optical aberrations that are created by tissues. To mitigate such effects, the use of high-energy excitation pulses² trades increased depth for the risk of nonlinear photodamage, while the use of an underfilled objective aperture³ sacrifices spatial resolution for increased depth. Alternatively, adaptive optics (AO)⁴ can improve multiphoton imaging by synthesizing a distortion to the wavefront of the excitatory beam that compensates for tissue-induced aberrations in the wavefront. The desired excitation wavefront can be determined using direct^{5–7} or indirect^{8–10} methods of wavefront sensing. Direct sensing of the wavefront from a descanned guidestar signal leads to wavefront correction with high photon and time efficiency^{5,7}. A previous application of this approach, in which exogenous dye was injected into mouse cortex to form the guidestar, enabled the determination of spine geometry up to 600 μm below the pia and functional imaging of spines down to 500 μm below the pia⁷ (Supplementary Fig. 1), that is, in granular but not infragranular layers, in an acute preparation. An unmet challenge is to develop a robust imaging paradigm to resolve axons and spines throughout infragranular layers, which encompass all output neurons from the neocortex to other brain areas, including premotor neurons.

We developed an approach that generates a guidestar from two-photon excitation of cyanine5.5-conjugated 2-MDa dextran (Cy5.5-dextran) within microvessels (Fig. 1 and Supplementary Figs. 2 and 3). Cy5.5 has strong two-photon absorbance at 1.25 μm and emission that peaks at 710 nm. In the approach, Cy5.5-dextran is delivered by retro-orbital injection and spreads into all vessels in the body. Unlike dye injected into a region of the brain⁷, Cy5.5 is constantly replenished in brain vasculature, is nontoxic and is compatible with use in chronic studies with closed cranial windows¹¹ or thinned-skull transcranial imaging¹² (Fig. 1b and Supplementary Video 1). We use descanned direct wavefront sensing (Fig. 1a), achieving robust measurements of aberrations across the target region, typically a square of 50 to 100 μm on edge, by exciting labeled microvessels within the tar-

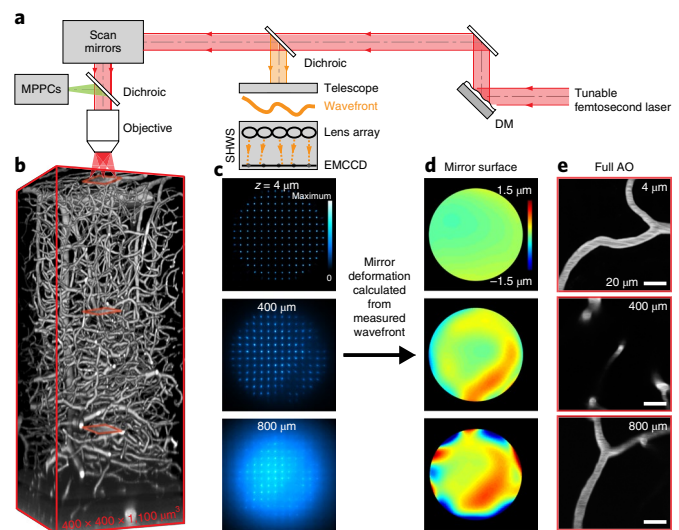


Fig. 1 | Aberration measurements up to 800 μm below the pia in the parietal cortex of an awake mouse using wavefront sensing from a microvascular-based guidestar. a, Adaptive optical two-photon microscopy using direct wavefront sensing from the descanned signal of a guidestar, which is formed by two-photon excitation of Cy5.5 in the vasculature lumen, with a SHWS. The wavefront is corrected by a DM. The signal for brain imaging is detected by MPPCs. **b**, In vivo two-photon imaging of vasculature in a $400 \times 400 \times 1,100 \mu\text{m}^3$ volume of cortex with blood plasma labeled with Cy5.5-dextran. The excitation wavelength was $\lambda = 1.25 \mu\text{m}$. Red boxes indicate three example subregions used for wavefront sensing in **c**. **c**, Spot patterns formed by the wavefront sensor from the descanned guidestar signal; the distance of each spot from its central position determines the tilt of the wavefront. **d**, Wavefront maps reconstructed using the spot patterns from the wavefront sensor at different depths. **e**, Microvessels at 14, 400 and 800 μm below the pia (red boxes in **b**) form the guidestars by two-photon excitation.

get region. The wavefront of the descanned light from the guidestar is analyzed by a Shack–Hartmann wavefront sensor (SHWS) that incorporates an electron multiplying charge-coupled device (EMCCD) and produces a pattern of spots whose individual positions demarcate the tilt of a subregion of the wavefront (Fig. 1a,c and Supplementary Fig. 4a,b). This pattern serves as input to a reconstruction algorithm that weights the input according to the signal-to-background ratio of each spot (Supplementary Fig. 4c,d) and then specifies the shape of the deformable mirror (DM). The DM alters the wavefront of the excitation beam to approximate

¹Department of Physics, University of California at San Diego, La Jolla, CA, USA. ²Howard Hughes Medical Institute, Janelia Research Campus, Ashburn, VA, USA. ³Section of Neurobiology, University of California at San Diego, La Jolla, CA, USA. *e-mail: dk@physics.ucsd.edu

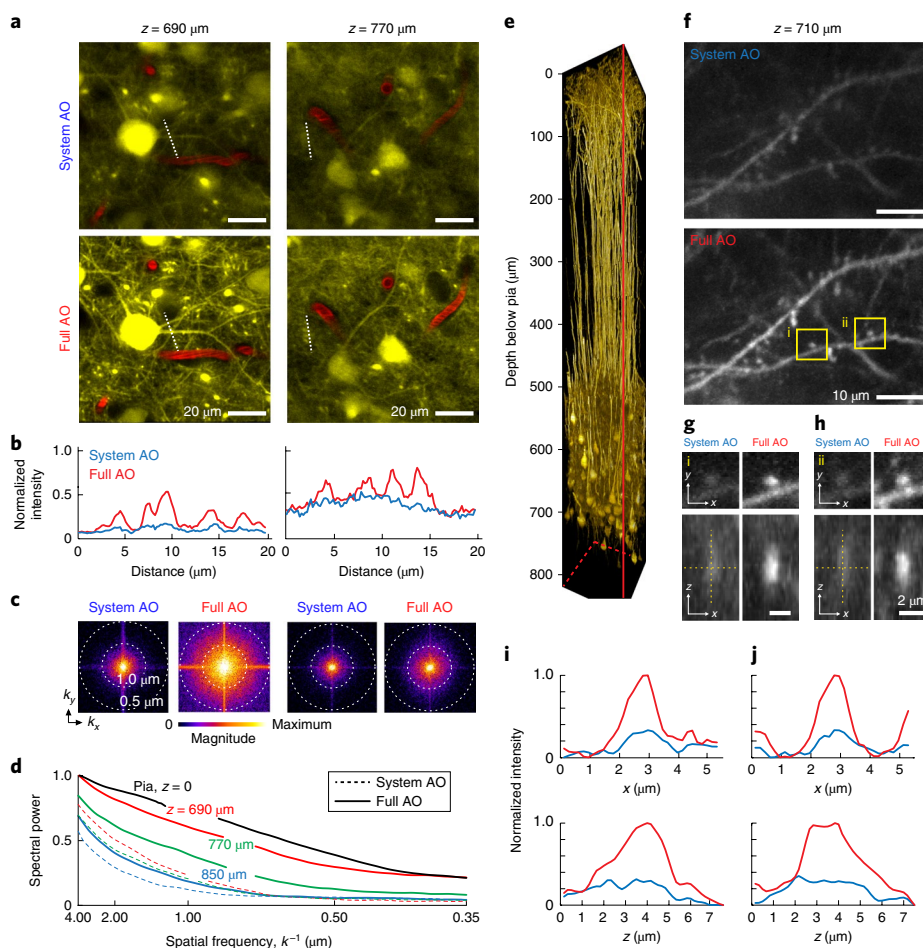


Fig. 2 | AO correction with wavefront sensing from microvessels enables imaging of dendritic spines in layer 5 of mouse vS1 cortex in vivo. **a**, Matrix of images at 690 μm (left) and 770 μm (right) below the pia in vS1 cortex with system or full AO correction. Data were obtained from a Thy1-YFP SLICK A mouse using excitation wavelength $\lambda = 1.04 \mu\text{m}$. **b**, Signal profiles along the dashed lines in **a** enable a comparison of corrections from system AO (blue line) and full AO (red line). **c**, Spectral power as a function of spatial frequency k for the images in **a**. **d**, $|k|$ -space plot of the spatial frequency from images at depths of 690, 770 and 850 μm below the pia with system AO (dashed lines) and full AO (solid lines) correction. Data are from **a**, **c** and Supplementary Fig. 6b–d. **e**, In vivo imaging of mRuby2-labeled layer 5 pyramidal neurons in a $150 \times 150 \times 810 \mu\text{m}^3$ volume of vS1 cortex at excitation wavelength $\lambda = 1.07 \mu\text{m}$. The virus AAV-Flex-mRuby2 was injected into layer 5 of Rbp4-Cre KL100 mice. Full AO corrections were applied at every 50 μm of depth. **f**, Imaging of dendritic spines at 710 μm below the pia in the same mouse as in **e** with system (top) and full (bottom) AO correction. **g, h**, Magnified views of postsynaptic spines corresponding to the boxed regions in **f**. The spines are shown in lateral and axial views. **i, j**, The x and z profiles of intensity for spines corresponding to the boxed regions in **f**.

a diffraction-limited focus inside the sample (Fig. 1d). We use light with a wavelength of $1.25 \mu\text{m}$ to excite the guidestar and to measure blood flow, while we use light at shorter wavelengths to excite indicators of subcellular structure and function. This avoids photobleaching of nonrenewable indicators during measurement of the tissue-induced aberrations. Emission from the indicators is detected with multipixel photon counters (MPPCs; Supplementary Fig. 3).

We evaluated our approach in the primary vibrissa sensory (vS1) cortex of adult mice using a closed cranial window and a two-photon microscope (Supplementary Figs. 2 and 3). In the approach, aberrations induced by imperfections in the microscope and the cranial window are nulled by a gradient-descent method. Attenuation of the ballistic light leads to a decrease in the signal-to-background ratio of the SHWS pattern of spots and limits the depth for effective wavefront measurement to 850 μm below the pia (Supplementary Fig. 4). We refer to correction of aberrations within the microscope and cover glass as ‘system AO’ and correction of all aberrations, including those from brain tissue, as ‘full AO’.

We first performed in vivo morphological imaging in mice that exhibited dense labeling of projection neurons with yellow fluorescent protein (YFP) (Thy1-YFP SLICK A mice). Images obtained with full AO correction contained fine dendritic structures in deep cortical layers that could not be resolved with system AO correction alone, at a depth of either 690 μm or 770 μm below the pia (Fig. 2a and Supplementary Video 2). The improvement is highlighted by line profiles through the fine processes (Fig. 2b) and line scans of the shadows of red blood cells flowing in capillaries (Supplementary Fig. 5). Maps of the spectral power density showed that higher spatial frequencies, k , were substantially restored by full AO correction (Fig. 2c). For a quantitative assessment of the depth limits for AO correction, we compared the power in the spatial frequency distribution between full AO and system AO correction at the level of the pia to the power at depths of 690, 770 and 850 μm below the pia (data from three mice; Fig. 2d). We achieved near-diffraction-limited resolution with full AO correction up to 700 μm below the pia and enhanced imaging of fine structures up to 850 μm below the pia (Fig. 2 and Supplementary Figs. 5–7).

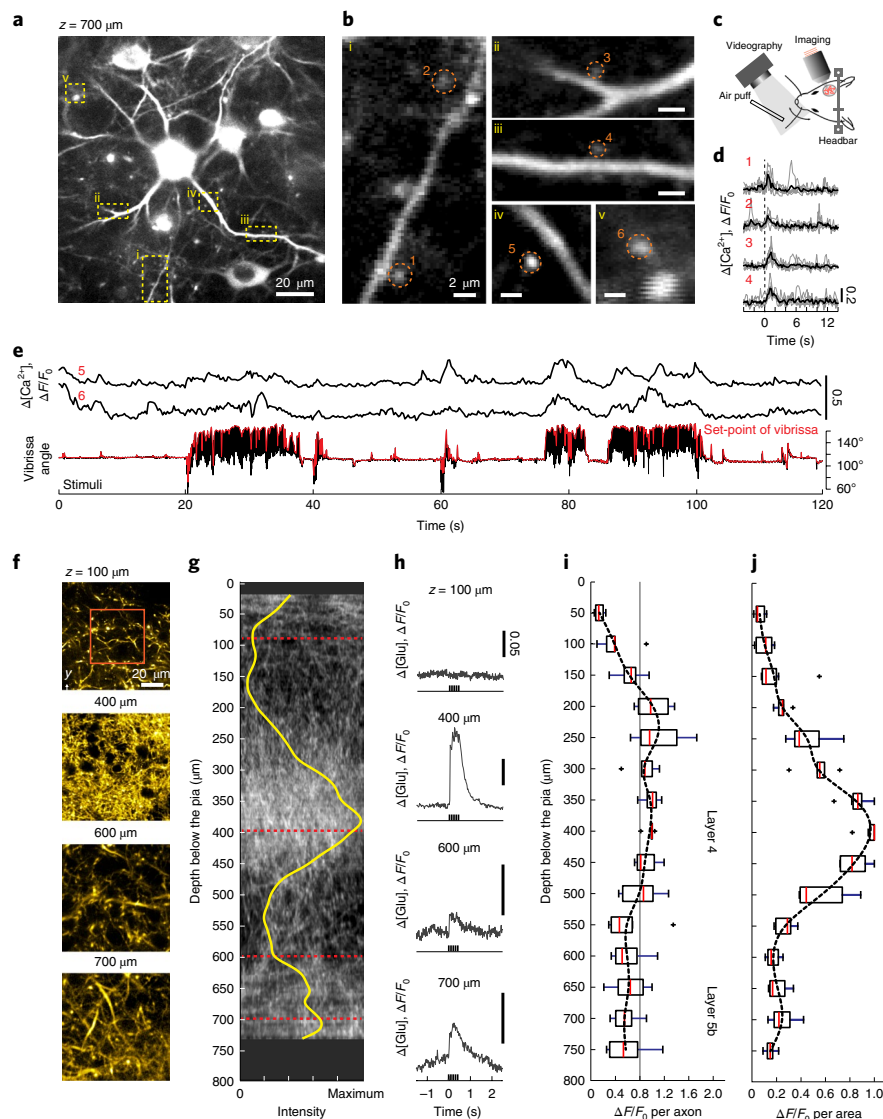


Fig. 3 | In vivo imaging of calcium and glutamate signaling in dendritic spines and thalamocortical axons in deep layers of vS1 cortex with full AO correction. **a**, Calcium imaging of layer 5b basal dendrites and spines at 700 μm below the pia in vS1 cortex at excitation wavelength $\lambda = 1.07 \mu\text{m}$. The virus AAV-Flex-jRGECO1a was injected into layer 5 of Rbp4-Cre KL100 mice. **b**, Expanded views of the areas enclosed by the dashed boxes in **a**. **c**, Schematic of vibrissa tracking with a high-speed camera and air-puff stimulation during imaging. **d**, **e**, Intracellular calcium response of dendritic spines enclosed by the red dashed circles in **b** to air-puff stimulation of the C2 vibrissa. The vibrissa was held without whisking in **d** and with free whisking in **e**. For the latter case, the concurrent vibrissa angle (black) and set-point (red) during epochs of rhythmic whisking and quiescence are shown. The experiments were repeated in three mice with similar results. **f**–**j**, Imaging of thalamocortical axons to measure the activation of SF-Venus-iGluSnFR.A184S by glutamate release in response to air-puff stimulation of vibrissae. Thalamocortical axons were labeled by injection of SF-Venus-iGluSnFR.A184S into the barreloids of ventral posterior medial thalamus and imaged at excitation wavelength $\lambda = 1.03 \mu\text{m}$. The glutamate response was measured every 50 μm from 50 μm to between 730 and 750 μm below the pia in the cortical columns for vibrissae in vS1 cortex. **f**, Example axon images for the B2 vibrissa cortical column (Supplementary Fig. 9d). **g**, A 175- μm -thick projection in the x–z plane for one animal and the density (yellow) as an average over all images. **h**, Time-dependent signal of glutamate release corresponding to **g**, averaged over the region outlined by the red box in **f**. **i**, **j**, Glutamate responses throughout the measurable depth of the cortical columns for the C1, C2, B2 and B3 vibrissae are shown as a population average of the peak amplitude of the signal per axon (**i**) or per area (**j**). The gray line serves as a guide for a possible mean response. Box plots in **i** and **j** are shown as the maximum, minimum, third quartile, first quartile and median ($n = 7$). Experiments were carried out on seven cortical columns across four mice.

We specifically labeled projection neurons with mRuby2 in deep cortical layers of Rbp4-Cre KL100 mice (Fig. 2e). Basal dendritic spines were resolved at 710 μm below the pia (Fig. 2f). Intensity and resolution in both the lateral and axial directions were substantially enhanced and approach the diffraction limit after full AO correction (Fig. 2g–j). Furthermore, using axial and lateral tiling of contiguous sub-regions in the cortex, we obtained full AO correction

for volumes that were up to 810 μm in depth and 300 μm on edge (Supplementary Figs. 7a and 8).

We then applied direct wavefront sensing to study pre- and post-synaptic responses in layer 5b of vS1 cortex during active tactile sensing. We imaged calcium transients in the spines of basal dendrites in layer 5b pyramidal neurons in Rbp4-Cre KL100 mice that expressed jRGECO1a¹³ (Fig. 3a,b and Supplementary Video 3), and reported

the fractional change in fluorescent emission, $\Delta F/F_0$, where $\Delta F = F(t) - F_0$, and F_0 is the baseline fluorescence. At the same time, we measured whisking in response to air-puff stimulation of the vibrissae (Fig. 3c). Basal dendritic spines produced either robust calcium transients in response to the onset of stimulation (Fig. 3d) or tonic responses concurrent with slow changes in the set-point of the angle of the vibrissae during whisking (Fig. 3e). These results imply that infragranular layers in vS1 receive both input from vibrissa touch, via the lemniscal pathway, and efferent copy input of self-motion.

We imaged glutamate release from presynaptic thalamocortical axons, using SF-Venus-iGluSnFR.A184S¹⁴ expressed in thalamocortical neurons, to quantify the nature of input to layer 5b neurons in vS1 cortex (Fig. 3f,g and Supplementary Fig. 9). We measured the SF-iGluSnFR basal fluorescence every 50 μm from the surface to a depth of between 730 and 750 μm below the pia and found peaks of fluorescence in layers 4 and 5b (Fig. 3g), consistent with morphological studies in rat¹⁵. In response to vibrissa stimulation of mice, we observed reliable signals of glutamate release in granular and infragranular layers (Fig. 3h and Supplementary Fig. 9d) with a near-constant release for each axon throughout the depth of the cortex (seven columns across four mice; Fig. 3i). The greater release per area in layer 4 (Fig. 3j) is consistent with the higher density of axonal boutons in layer 4. These functional data support the consideration of layer 5b as a second thalamocortical projection hub in vS1 cortex¹⁶.

We then performed chronic transcranial imaging in a thinned-skull preparation. Despite the large aberration, we reliably imaged the vasculature and red blood cell flux up to a depth of 600 μm below the pia with improved spatial resolution and increased brightness with full AO as compared to system AO (three mice; Supplementary Fig. 10). Full AO correction restored the spatial frequency of neuronal images over wide fields (Supplementary Fig. 11a–h) and to deeper regions (three mice; Supplementary Fig. 11i), which allowed us to detect spontaneous calcium spikes from bright processes up to 520 μm below the pia in Thy1-jRGECO1a mice (Supplementary Fig. 12).

Finally, we considered potential effects of phototoxicity on physiological function during long-term deep-imaging studies with full AO correction^{17–19}. For continuous imaging of glutamate from axons or calcium increases in dendrites and spines, we observed no change in functional response over 30 min for a typical power at the focus (approximately 5 mW; Supplementary Figs. 13 and 14). We similarly did not observe degradation of the response on subsequent days (Supplementary Fig. 13). We evaluated the dependence of phototoxicity on power in the case of flow of red blood cells in vessels with Cy5.5-labeled plasma. We observed a stable flow rate at power at or below 10 mW and degradation in the form of stalls²⁰ only for power near or above 20 mW (Supplementary Fig. 15). We observed neither tissue damage nor photobleaching. We conclude that, using full AO correction, we can achieve long-term chronic recording.

We have shown that direct wavefront sensing enables functional imaging of subcellular components up to 850 μm below the pia in the adult mouse brain. Substantially deeper imaging will require the use of longer excitation wavelengths and, thus, three- rather than two-photon excitation²¹. Here greater optical penetration is traded against the lower cross-section for three-photon absorption and the need for higher pulse energies, albeit with a risk of photodamage¹⁹.

Online content

Any methods, additional references, Nature Research reporting summaries, source data, statements of code and data availability and

associated accession codes are available at <https://doi.org/10.1038/s41592-019-0434-7>.

Received: 17 November 2018; Accepted: 29 April 2019;

Published online: 17 June 2019

References

- Svoboda, K., Denk, W., Kleinfeld, D. & Tank, D. W. *Nature* **385**, 161–165 (1997).
- Mittmann, W. et al. *Nat. Neurosci.* **14**, 1089–1093 (2011).
- Kondo, M., Kobayashi, K., Ohkura, M., Nakai, J. & Matsuzaki, M. *eLife* **6**, e26839 (2017).
- Ji, N. *Nat. Methods* **14**, 374–380 (2017).
- Tao, X. et al. *Opt. Lett.* **36**, 1062–1064 (2011).
- Wang, K. et al. *Nat. Methods* **11**, 625–628 (2014).
- Wang, K. et al. *Nat. Commun.* **6**, 7276 (2015).
- Ji, N., Milkie, D. E. & Betzig, E. *Nat. Methods* **7**, 141–147 (2010).
- Débarre, D. et al. *Opt. Lett.* **34**, 2495–2497 (2009).
- Tang, J., Germain, R. N. & Cui, M. *Proc. Natl Acad. Sci. USA* **109**, 8434–8439 (2012).
- Holtmaat, A. et al. *Nat. Protoc.* **4**, 1128–1144 (2009).
- Drew, P. J. et al. *Nat. Methods* **7**, 981–984 (2010).
- Dana, H. et al. *eLife* **5**, e12727 (2016).
- Marvin, J. S. et al. *Nat. Methods* **15**, 936–939 (2018).
- Oberlaender, M. et al. *Cereb. Cortex* **22**, 2375–2391 (2011).
- Castro-Alamancos, M. A. & Connors, B. W. *Prog. Neurobiol.* **51**, 581–606 (1997).
- Hopt, A. & Neher, E. *Biophys. J.* **80**, 2029–2036 (2001).
- Laissue, P. P., Alghamdi, R. A., Tomancak, P., Reynaud, E. G. & Shroff, H. *Nat. Methods* **14**, 657–661 (2017).
- Yildirim, M., Sugihara, H., So, P. T. C. & Sur, M. *Nat. Commun.* **11**, 177 (2019).
- Kleinfeld, D., Mitra, P. P., Helmchen, F. & Denk, W. *Proc. Natl Acad. Sci. USA* **95**, 15741–15746 (1998).
- Ouzounov, D. G. et al. *Nat. Methods* **14**, 388–390 (2017).

Acknowledgements

We acknowledge N. Ji, C. Xu and J. Kubby for detailed advice on deep imaging; T. Komiya (UCSD) for the gift of transgenic mice; B. Lim (UCSD) for the gift of viruses; M. Thunemann for instruction on synthesis of Cy5.5–dextran; C. Foo for assistance with the motion-correction algorithm; A. Lozada and C. Mateo for advice on surgery; M. Deschênes, M. Häusser, B. Strowbridge and K. Svoboda for discussions; and B. Friedman for comments on an early version of the manuscript. Design and fabrication of the microscope were supported by the National Science Foundation (MRI grant PHY153264) and physiological measurements were additionally supported by the National Institutes of Health (NINDS grant R35 NS097265).

Author contributions

D.K. and R.L. designed the instrument, planned the experiments and wrote the manuscript; R.L. fabricated the instrument and performed all experiments; Z.L. coded the reconstruction algorithm and assisted with initial experiments; J.S.M. synthesized the glutamate sensor; and D.K. ensured that all university rules and forms that govern environmental health and safety, including the ethical use of animals as well as the use of chemicals, controlled substances, hazardous substances, lasers and viruses were complied with.

Competing interests

The authors declare no competing interests.

Additional information

Supplementary information is available for this paper at <https://doi.org/10.1038/s41592-019-0434-7>.

Reprints and permissions information is available at www.nature.com/reprints.

Correspondence and requests for materials should be addressed to D.K.

Publisher's note: Springer Nature remains neutral with regard to jurisdictional claims in published maps and institutional affiliations.

© The Author(s), under exclusive licence to Springer Nature America, Inc. 2019

Methods

Microscope design. A femtosecond laser beam with a tunable wavelength from 680 nm to 1,300 nm (Coherent, Chameleon Discovery) was passed through a Pockels Cell (Conoptics, 350-105-02 (cell) and 302 (driver)) for power modulation (Supplementary Fig. 2a). Group delay dispersion was precompensated by the laser's built-in dispersion compensation unit at wavelengths of 1,030 nm, 1,040 nm, 1,070 nm and 1,250 nm. The beam was expanded tenfold by lens pair L1 and L2 (Newport, KPX094AR.18 ($f=100$ mm) and KPX124AR.18 ($f=1,000$ mm)) to slightly overfill the aperture of the DM (Alpao, DM97-15). The excitation beam reflected by the DM was compressed threefold by a 4*f* telescope formed by L3 and L4 (Newport, KPX119AR.18 ($f=600$ mm) and KPX106AR.18 ($f=200$ mm)), the DM and galvo *y* were conjugated. Translation stage 1 (TS1), TS2, and TS3 carry TS2 and M1, DM and M2, and M3 and M4, respectively. M3 and M4 can be adjusted to ensure the alignment of the 4*f* telescope between the DM and galvo *y*. Galvos *x* and *y* (Cambridge Technology, 5-mm mirror 6215H) were conjugated by a 4*f* relay formed by lens pair L5 and L6, both of which consist of two achromatic doublets (Thorlabs, AC508-150-B ($f=150$ mm)). The back focal plane of the objective (Olympus, XLPLN25XSVMP2, $\times 25$, 1.0 NA and 4-mm working distance) and galvo *x* were conjugated by a 4*f* telescope formed by scan lens L7 and tube lens L8. L7 consists of a plano-concave lens (Newport, KPC070AR.16 ($f=-200$ mm)), a bi-convex lens (Thorlabs, LB1199-B ($f=200$ mm)) and two achromatic doublets (Thorlabs, AC508-150-B ($f=150$ mm)). Tube lens L8 was formed by two achromatic doublets (Thorlabs, AC508-500-B ($f=500$ mm)). The beam reflected by galvo *x* was expanded 3.25-fold before incidence into the objective.

The fluorescence emission signal for imaging was reflected by primary dichroic D1 (Semrock, FF665-Di02-35 \times 37; FF775-Di01-25 \times 36 switched to Cy5.5 imaging) to three different channels, which were spectrally isolated by dichroic mirrors D2 (Semrock, FF552-Di02-25 \times 36) and D3 (Semrock, FF662-Di01-25 \times 36) and emission filters F1 (Semrock, FF01-530/55-25) for the green/yellow channel, F2 (Semrock, FF01-593/46-25) for the red channel and F3 (Semrock, FF01-708/75-25) for the far-red channel. A fluorescence-collection system built with off-the-shelf lenses (Thorlabs, LA1765-A, LA1805-A, LA1027-A and A240-A; Supplementary Fig. 3) coupled with the MPPCs (Hamamatsu, C13366-3050GA) allowed the imaging signal to be detected with high efficiency.

In wavefront sensing mode, the emission signal from the guidestar transmitted through D1 and was descanned by galvos *x* and *y*. The guidestar emission signal was separated from the excitation beam by dichroic mirror D4 (Semrock, FF775-Di01-25 \times 36) and expanded 1.5-fold by a 4*f* relay formed with L9 and L10 (Thorlabs, AC254-100-A ($f=100$ mm) and AC254-150-A ($f=150$ mm)) before arriving at the microlens array (Edmund, 64-483) of the SHWS. The SHWS camera (Andor, iXon Ultra 888) was placed at the focal plane of the microlens array to acquire an image of the guidestar spots. Note that the DM, galvos, back focal plane of the objective and SHWS microlens array were all located in the same conjugate plane.

The imaging system was controlled by ScanImage (Vidrio Technologies) running on Matlab (Mathworks). Signals from MPPCs were amplified twice by a voltage preamplifier (Stanford Research Systems, SR445A) and subjected to antialias filtering before digitization (National Instruments, PCI-6110). A custom Matlab program integrated with ScanImage was built to control the DM and the SHWS camera. Custom Matlab code was made for system AO calibration, system-aberration calibration and measurement of sample aberrations.

Detectors. The MPPCs used in this study are solid-state single-photon-sensitive detectors implemented by 60 \times 60 Geiger-mode avalanche photodiode pixels with a pitch of 50 μ m. The effective photosensitive area is 3 mm by 3 mm with a spectral response up to 900 nm. The MPPCs provide extremely low multiplicative noise as compared to photomultiplier tubes²², high sensitivity and a linear response for the typical number of photons emitted per laser pulse²³. In this study, the MPPCs operate in analog mode after passing the antialiasing filter.

System AO calibration. The DM was precalibrated in the factory such that commands for a flat mirror and commands to drive each of the first 60 of Noll's Zernike modes²⁴ at 1- μ m root-mean-square amplitude are provided with the instrument. These transform each of the 60 Zernike modes into command voltages for each of 97 actuators which is denoted Z2C, where

$$\mathbf{Z}2\mathbf{C} = \begin{pmatrix} v_{1,1} \cdots v_{1,97} \\ \vdots \\ v_{60,1} \cdots v_{60,97} \end{pmatrix}$$

The SHWS and DM are calibrated with respect to each other after the system is well aligned. First, the objective is replaced by a flat mirror in the back focal plane. The calibration beam is incident on the DM, reflected by the pupil mirror and finally projected into the SHWS. The DM flat command is applied to obtain a wavefront spot pattern for calibration reference. Then, each of the 60 individual Zernike modes is displayed by the DM, and the deflection of the result spots on the SHWS, which correspond to changes on the wavefront of the DM, is

recorded. The vector of the center location of spots in the flat reference pattern \mathbf{S}_{Cref} where

$$\mathbf{S}_{\text{Cref}} = \begin{pmatrix} \underbrace{S_{\text{Cref}1} \cdots S_{\text{Cref}N}}_{\text{shifts on } x}, \underbrace{S_{\text{Cref}N+1} \cdots S_{\text{Cref}2N}}_{\text{shifts on } y} \end{pmatrix}$$

and the 60 Zernike modes patterns \mathbf{S}_{Cz} , where

$$\mathbf{S}_{\text{Cz}} = \begin{pmatrix} S_{\text{Cz}1,1} \cdots S_{\text{Cz}1,2N} \\ \vdots \\ S_{\text{Cz}60,1} \cdots S_{\text{Cz}60,2N} \end{pmatrix},$$

are determined by a Gaussian-fit centroid algorithm²⁵ to achieve subpixel precision; there are 60 \times *N* elements in the array, where *N* is the number of spots in each waveform pattern, and each element has two entries, that is, the *x* and *y* shift from the center. The spot-shift array of the flat reference is subtracted from each of the 60 spot-shift arrays for the different Zernike modes. This yields a 60 \times *N* calibration matrix \mathbf{S}_{B} that stores the spot shifts on the SHWS that correspond to phase shifts for each Zernike mode at 1- μ m root-mean-square amplitude on the DM, with elements $S_{\text{B}ij} = S_{\text{Cz}ij} - S_{\text{Cref}j}$.

System aberration calibration. System aberration refers to imperfections of the microscope as well as the aberration induced by the coverslip of the cranial window. These are calibrated at the wavelength of 1,070 nm and 1,250 nm by imaging the central 100 μ m \times 100 μ m field of a 2–5% aqueous fluorescent solution of sulforhodamine B or sulfo-cyanine5.5 NHS ester (Sulfo-Cy5.5) (Lumiprobe, 27320) with a number 1 coverslip on top. We use a gradient-descent algorithm to optimize the amplitude of the different Zernike modes that are displayed by the DM to maximize the average intensity (Supplementary Fig. 2b,c). In each optimization cycle, the increments of the Zernike mode coefficients were computed on the basis of the gradient of mean intensity changes so that current Zernike modes kept on updating. Usually after 20 cycles of optimization the coefficients of the Zernike mode became stable. Tip, tilt and defocus were excluded in this calibration. This leads to a point spread function with full widths at half maximum of 0.5 μ m and 2 μ m in the lateral and axial directions, respectively, at 1,070-nm wavelength, measured using 200-nm fluorescent beads (Supplementary Fig. 2d). We found that this procedure also leads to a near minimum point-spread function in off-center regions, for example, across the entire 700 μ m \times 700 μ m field, albeit with some field curvature of the focal surface. The result of this procedure is a single stable DM command \mathbf{C}_{Sy} for system aberration correction, where $\mathbf{C}_{\text{Sy}} = (C_{\text{Sy}1} \cdots C_{\text{Sy}97})$.

Sample aberration measurement. Sample aberrations are caused by brain tissue. A reference pattern of spots on the SHWS was recorded using the aqueous solution of Sulfo-Cy 5.5. Then we measured the wavefront in samples that fluoresced from any location along blood vessels labeled with Cy5.5-dextran, using the descanned voxels as a guidestar. The spot locations of the sample aberration \mathbf{S}_{M} , where $\mathbf{S}_{\text{M}} = (S_{\text{M}1} \cdots S_{\text{M}2N})$, and the reference \mathbf{S}_{Sref} , where $\mathbf{S}_{\text{Sref}} = (S_{\text{Sref}1} \cdots S_{\text{Sref}2N})$, were determined using the centroid algorithm described above. The relative location shift between the sample spots and reference spots was then calculated, which represents the sample aberration \mathbf{S}_{S} , where $\mathbf{S}_{\text{S}} = \mathbf{S}_{\text{M}} - \mathbf{S}_{\text{Sref}}$. The sample spot-shift array is decomposed into the calibration basis \mathbf{S}_{B} that was obtained previously to generate the 60-mode Zernike coefficient \mathbf{Z}_{S} , where $\mathbf{Z}_{\text{S}} = (\mathbf{S}_{\text{B}})^{\dagger} (\mathbf{S}_{\text{S}})^{\top}$ or $\mathbf{Z}_{\text{S}} = (\mathbf{W} \mathbf{S}_{\text{B}})^{\dagger} (\mathbf{W} \mathbf{S}_{\text{S}})^{\top}$. For the second version of \mathbf{Z}_{S} , a weighting matrix \mathbf{W} is calculated on the basis of the signal-to-background ratio of each spot in the SHWS image (Supplementary Fig. 4e). The generalized matrix inverse is indicated by $(\cdots)^{\dagger}$. For aberration correction, tip and tilt were excluded. The DM command for correcting sample aberration is then calculated as \mathbf{C}_{S} , where $\mathbf{C}_{\text{S}} = -\mathbf{Z}_{\text{S}} \mathbf{Z}2\mathbf{C}$. To display the wavefront that we measured from the sample, modal wavefront reconstruction with Zernike polynomials was performed²⁶.

Full AO correction. The DM command for the system and sample corrections are added for the final correction. The sample correction is applied to isoplanatic regions that vary between 50 μ m and 100 μ m in side length. The full AO correction is denoted $\mathbf{C} = \mathbf{C}_{\text{S}} + \mathbf{C}_{\text{Sy}}$.

Animal preparation. All experiments were conducted on adult male mice (>8 weeks old). Wild-type mice (C57BL/6J) and transgenic mice (Tg(Rbp4-Cre)KL100Gsat²⁷, referred to in the text as Rbp4-Cre KL100 mice; Tg(Thy1-jRGECO1a)GP8.31Dkim/J²⁸, referred to in the text as Thy1-jRGECO1a mice; and B6.Cg-Tg(Thy1-YFP-SLICK A)AGfng/J²⁹, referred to in the text as Thy1-YFP SLICK A mice) were used. All experimental procedures on our animals were performed in accordance with the Guide for the Care and Use of Laboratory Animals and have been approved by the Institutional Animal Care and Use Committee at the University of California, San Diego (UCSD).

Mice were anesthetized with isoflurane using a precision vaporizer, 3% (vol/vol) in oxygen for induction and 1–2% (vol/vol) for maintenance. Body

temperature was maintained at 37°C with a heating pad with a feedback monitor during anesthesia. The animal was then given analgesic buprenorphine subcutaneously (0.1 µg per gram body weight) and placed in a stereotaxic frame. The scalp was removed in a sterile fashion and the periosteum on the parietal and occipital plates was removed gently.

Chronic cranial window. A 4-mm-diameter craniotomy was made over the right vS1 cortex (centroid at 1.5 mm posterior to the bregma and 3.4 mm lateral from the midline). Dura was left intact. An imaging window^{11,30} was constructed using a single 4-mm round coverslip (number 1, 170 µm thick) that was embedded in the craniotomy and sealed around the edge with cyanoacrylate glue (Loctite, cat. no. 401). Dental acrylic (Lang Dental) was further applied around the edge of the coverslip to reinforce stability. A titanium headbar was glued onto the skull with Meta-bond (Parkell) for head fixation. The remaining exposed bone and the headbar on top of the region were covered with dental acrylic to increase stability.

Chronic thinned-skull window. A 3-mm-diameter region of skull over the right vS1 cortex was thinned down to a thickness of between 50- and 100-µm thick with a 250-µm drill bur^{12,31}. The thinned bone was dried and covered with cyanoacrylate glue and a 4-mm round coverslip. All other procedures were the same as for cranial window surgery.

Virus injection. Virus injection was conducted before the circular craniotomy was made. To label the pyramidal neurons of layer 5 in vS1 cortex, virus containing jRGECO1a (AAV2/1.Syn.Flex.NES-jRGECO1a.WPRE.SV40, Penn Vector Core; genomic titer, 4.48×10^{13} ; dilution factor, 6:1) or mRuby2 (ref. ³²) (AAV2/1.hSyn.DIO.mRuby2, UCSD; genomic titer, 8.8×10^{12}) was injected (50 nl, 10 nl min⁻¹) at a 45° angle into the target coordinates of the cortex of Rbp4-Cre mice, 1.5 mm posterior to Bregma, 3.4 mm lateral from the midline and at a depth of 0.7 mm. To label the thalamocortical projections in vS1 cortex, virus expressing SF-Venus-iGluSnFR (AAV2/1.hSyn.Flex.SF-Venus-iGluSnFR.A184S, Janelia Research Campus; genomic titer, 1×10^{13}) was mixed with AAV-Cre (AAV2/1.hSyn.Cre.WPRE.hGH, Addgene; genomic titer, 1×10^{13} ; dilution factor, 1:100) in a 1:1 ratio and injected (50 nl, 10 nl min⁻¹) perpendicularly to the barreloids of ventral posteromedial nucleus in wild-type mice, 1.7 mm posterior to the bregma, 1.7 mm lateral from the midline and at a depth of 3.0 mm. For all injections glass pipettes (Drummond) were pulled and beveled to a sharp tip (30-µm outer diameter) and a syringe pump (Kd Science, Legato 185) was used to control the infusion.

In vivo imaging. Imaging was performed 7 d after the cranial window surgery or 14–21 d after cranial window surgery with virus injection. Animals with thinned skull windows were imaged 3–5 d after the surgery. Animals were handled and trained for head fixation for 1 h daily for 3 d ahead of imaging. Cy5.5 NHS ester (Lumiprobe, 27020) was conjugated with amino-dextran 2,000 kDa (Finabio, AD2000 × 200) to obtain a 5% (wt/vol) solution in PBS of Cy5.5–dextran. Before imaging, mice were briefly anesthetized with isoflurane to label the lumen of blood vessels via a retro-orbital intravenous injection of 50 µl Cy5.5–dextran in PBS³³. The cranial window was carefully aligned perpendicularly to the objective axis using a mouse positioner based on a goniometer stage (Thorlabs, GNL20).

During wavefront sensing, the laser was tuned to 1,250 nm and the average incident power through the objective ranged from 4 to 135 mW depending on depths in all experiments (Supplementary Table 1). Within an isoplanatic region, frame scanning over the whole field was alternated with scanning over multiple regions of interest on top of the microvessel to excite the guidestar signal. To image vasculature, the primary dichroic was switched to FF775-Di01-25×36. Post-objective power was <75 mW in all cranial-window experiments within a depth of 700-µm and a maximum power of 135 mW was used for imaging depths over 800 µm or in the thinned-skull-window experiments (Supplementary Table 2).

For neuronal imaging, the laser was tuned to 1,030, 1,040 and 1,070 nm to excite SF-Venus-iGluSnFR, enhanced YFP, and jRGECO1a and mRuby2, respectively. The imaging power post-objective was <165 mW in most experiments within a depth of 700 µm. Maximum imaging power was limited to 200 mW for imaging depths over 760 µm or in several mice that expressed SF-Venus-iGluSnFR at depth (Supplementary Table 3). Calcium imaging experiments with vibrissa stimulation and tracking were performed in awake animals. To image the glutamate response of thalamocortical axons to vibrissa stimulation, animals were under light anesthesia maintained by 1% (vol/vol) isoflurane in oxygen.

Vibrissa tracking and stimulation. One day before behavioral experiments, mice were pre-imaged under the two-photon microscope to check that virus was expressing in the vibrissa cortex. Locations in vS1 cortex were verified by intrinsic optical-signal imaging³⁴. Then, the animals were anesthetized and vibrissae were trimmed to between 10 and 15 mm, leaving only one or two vibrissae, that is, C1, C2, B2 and/or B3, whose cortical column had optimal expression of jRGECO1a or SF-Venus-iGluSnFR. The vibrissa was painted lightly with a white fabric paint. The experiments were carried out in the dark and the vibrissa was illuminated by an infrared LED source (Thorlabs, M940L3). A high-speed camera (Basler, acA1300-200um) was used to capture the whisking at 500 frames per second.

Air-puff deflection was used for vibrissa stimulation³⁵. During the stimulation sessions, pulse-controlled compressed air, 5 p.s.i. at the source, was delivered

through a fine tube, which was placed parallel to the side of the mouse snout and 10 mm away from the targeted vibrissa. Pulse width was 20 ms. The frequency of the air puffs was 10 Hz and the stimulation lasted for 500 ms in each trail.

Image analysis. All comparisons of system AO and full AO correction were performed with the same conditions including excitation laser power, imaging field, image size, pixel dwell time, frame average number (Supplementary Tables 1–3) and post-motion correction process.

Images were processed using MATLAB or ImageJ³⁶. Motion corrections were performed on mRuby2 or SF-Venus-iGluSnFR images using a Fourier-transform-based algorithm³⁷. Non-rigid motion corrections were performed on jRGECO1a calcium images and YFP images using nonRMCore³⁸ and on three-dimensional stacks of mRuby2 images using non-parametric image registration³⁹. Three-dimensional data were rendered using the '3D viewer' in ImageJ⁴⁰.

For calcium imaging data from spines (Fig. 3a,b), circular regions of interest were placed over individual dendrite spines to measure fluorescence. For the analysis of glutamate release per axon (Fig. 3i), the regions of axons were extracted using an intensity threshold.

To compute the signal enhancement ratio in neuronal morphological images (Supplementary Figs. 6e and 11i), line profiles were first extracted from selected fine processes and then the ratio of contrast, where contrast is defined as the difference between the peak and valley amplitudes of the signal, was calculated for system AO and full AO correction. A similar analysis was performed for the flux of red blood cells (Supplementary Figs. 5e and 10h).

Statistics. Box plots were used to show the signal-enhancement ratio between system AO and full AO correction of fine processes in neuronal morphological images and of the flux of red blood cells (Supplementary Figs. 5e, 6e, 10h and 11i).

To compare glutamate responses of thalamocortical axons in different cortical layers (Fig. 3i,j), we used box plots to show the amplitudes of glutamate responses across samples. A fitting curve using the mean response amplitude at each depth is also used to show the distribution trend.

Reporting Summary. Further information on research design is available in the Nature Research Reporting Summary linked to this article.

Data availability

The data that support the findings of this study are available from the corresponding author upon request. Source data are available online for Figs. 2 and 3 and Supplementary Figs. 5, 6, 10 and 11.

Code availability

The system aberration calculation, DM and SHWS calibration and sample-induced wavefront reconstruction and AO correction code are available in the Supplementary Software.

References

- Driscoll, J. D. et al. *J. Neurophysiol.* **104**, 1803–1811 (2011).
- Tsai, P. S. & Kleinfeld, D. in *Methods for In Vivo Optical Imaging* 2nd edn (ed. Frostig, R. D.) 59–115 (CRC Press, 2009).
- Noll, R. J. *J. Opt. Soc. Am.* **66**, 207–211 (1979).
- Thompson, R. E., Larson, D. R. & Webb, W. W. *Biophys. J.* **82**, 2775–2783 (2002).
- Cubalchini, R. *J. Opt. Soc. Am.* **69**, 973–977 (1979).
- Gong, S. et al. *Nature* **425**, 917–925 (2003).
- Dana, H. et al. *PLoS One* **13**, e0205444 (2018).
- Young, P. et al. *Nat. Neurosci.* **11**, 721–728 (2008).
- Morii, S., Ngai, A. C. & Winn, H. R. *J. Cereb. Blood Flow Metab.* **6**, 34–41 (1986).
- Shih, A. Y., Drew, P. J., Mateo, C., Kleinfeld, D. & Tsai, P. S. *J. Vis. Exp.* **61**, e3742 (2012).
- Lam, A. J. et al. *Nat. Methods* **9**, 105–112 (2012).
- Shih, A. Y. et al. *J. Cereb. Blood Flow Metab.* **32**, 1277–1309 (2012).
- Knutsen, P. M., Mateo, C. & Kleinfeld, D. *Philos. Trans. R. Soc. B* **371**, 20150351 (2016).
- Kleinfeld, D., Sachdev, R. N. S., Merchant, L. M., Jarvis, M. R. & Ebner, F. F. *Neuron* **34**, 1021–1034 (2002).
- Schindelin, J. et al. *Nat. Methods* **9**, 676–682 (2012).
- Guizar-Sicairos, M., Thurman, S. T. & Fienup, J. R. *Opt. Lett.* **33**, 156–158 (2008).
- Pnevmatikakis, E. A. & Giovannucci, A. *J. Neurosci. Methods* **291**, 83–94 (2017).
- Vercateren, T., Pennec, X., Perchant, A. & Ayache, N. *Neuroimage* **45**, S61–S72 (2009).
- Schmid, B., Schindelin, J., Cardona, A., Longair, M. & Heisenberg, M. *BMC Bioinformatics* **11**, 274 (2010).

Reporting Summary

Nature Research wishes to improve the reproducibility of the work that we publish. This form provides structure for consistency and transparency in reporting. For further information on Nature Research policies, see [Authors & Referees](#) and the [Editorial Policy Checklist](#).

Statistics

For all statistical analyses, confirm that the following items are present in the figure legend, table legend, main text, or Methods section.

n/a Confirmed

- The exact sample size (n) for each experimental group/condition, given as a discrete number and unit of measurement
- A statement on whether measurements were taken from distinct samples or whether the same sample was measured repeatedly
- The statistical test(s) used AND whether they are one- or two-sided
Only common tests should be described solely by name; describe more complex techniques in the Methods section.
- A description of all covariates tested
- A description of any assumptions or corrections, such as tests of normality and adjustment for multiple comparisons
- A full description of the statistical parameters including central tendency (e.g. means) or other basic estimates (e.g. regression coefficient) AND variation (e.g. standard deviation) or associated estimates of uncertainty (e.g. confidence intervals)
- For null hypothesis testing, the test statistic (e.g. F , t , r) with confidence intervals, effect sizes, degrees of freedom and P value noted
Give P values as exact values whenever suitable.
- For Bayesian analysis, information on the choice of priors and Markov chain Monte Carlo settings
- For hierarchical and complex designs, identification of the appropriate level for tests and full reporting of outcomes
- Estimates of effect sizes (e.g. Cohen's d , Pearson's r), indicating how they were calculated

Our web collection on [statistics for biologists](#) contains articles on many of the points above.

Software and code

Policy information about [availability of computer code](#)

Data collection

ScanImage 2016 running on MATLAB 2015a was used for two-photon imaging data collection. Code written in MATLAB was used to perform the AO wavefront sensing and correction. Pylon 5 from BASLER was used to control the animal behavior camera. Andor Solis was used to acquire image of the wavefront spots pattern during the wavefront sensing.

Data analysis

Fiji ImageJ was used for image average intensity projection. 3D Viewer in Fiji ImageJ was used for 3D rendering of structural stack images. Fiji ImageJ was also used for drawing the line profile ROI. MATLAB 2017b was used for image motion correction (e.g. rigid, and non-rigid correction) and further signal processing (e.g. line profile signal plotting, signal normalization, k-space calculating, box plot, and whisk mid-point filtering).

For manuscripts utilizing custom algorithms or software that are central to the research but not yet described in published literature, software must be made available to editors/reviewers. We strongly encourage code deposition in a community repository (e.g. GitHub). See the Nature Research [guidelines for submitting code & software](#) for further information.

Data

Policy information about [availability of data](#)

All manuscripts must include a [data availability statement](#). This statement should provide the following information, where applicable:

- Accession codes, unique identifiers, or web links for publicly available datasets
- A list of figures that have associated raw data
- A description of any restrictions on data availability

The original code, together with detailed instructions are available at the supplementary software.
Correspondence and requests for raw data should be addressed to D.K. (dk@physics.ucsd.edu).

Field-specific reporting

Please select the one below that is the best fit for your research. If you are not sure, read the appropriate sections before making your selection.

Life sciences Behavioural & social sciences Ecological, evolutionary & environmental sciences

For a reference copy of the document with all sections, see [nature.com/documents/nr-reporting-summary-flat.pdf](https://www.nature.com/documents/nr-reporting-summary-flat.pdf)

Life sciences study design

All studies must disclose on these points even when the disclosure is negative.

Sample size	A total number of 25 animals were involved in this study. For the morphological data showed in the study, we repeat imaging on 15 animals in total (closed cranial window and thinned skull window experiments) to ensure similar results are reproducible. For the functional study data, the imaging experiment were repeated on 4 animals for glutamate imaging and 3 animals for calcium imaging. For phototoxicity assessment the experiments were carried out on 3 animals. Over 500 times measurements were achieved across 15 animals for the morphological results in this study. Over 1200 trails of functional imaging were carried out across 7 animals. The animal surgery, experimental procedure and system operation are all standardized in this study. Animal brain states have minimum influence to the experiments in this study. Above all, we believe that the sample size in this study is sufficient for supporting the results.
Data exclusions	We only exclude the data whose quality was compromised by identifiable reasons, such as viral expression failure and cranial window surgery failure.
Replication	The results were based on sufficient sample size. We repeatable performed wavefront sensing and imaging down to 850 um deep on 3 animals. We showed the signal enhancement for both closed cranial window and thinned skull window experiments based the results from a total of 12 animals. For functional study, we repeat the thalamocortical axon imaging on 4 animals.
Randomization	No randomization was necessary in this study. Any experiment involving the comparison of imaging was done on the same cortical region of the same animal.
Blinding	No blinding was necessary since no group allocation was performed.

Reporting for specific materials, systems and methods

We require information from authors about some types of materials, experimental systems and methods used in many studies. Here, indicate whether each material, system or method listed is relevant to your study. If you are not sure if a list item applies to your research, read the appropriate section before selecting a response.

Materials & experimental systems

n/a	Involvement in the study
<input checked="" type="checkbox"/>	<input type="checkbox"/> Antibodies
<input checked="" type="checkbox"/>	<input type="checkbox"/> Eukaryotic cell lines
<input checked="" type="checkbox"/>	<input type="checkbox"/> Palaeontology
<input type="checkbox"/>	<input checked="" type="checkbox"/> Animals and other organisms
<input checked="" type="checkbox"/>	<input type="checkbox"/> Human research participants
<input checked="" type="checkbox"/>	<input type="checkbox"/> Clinical data

Methods

n/a	Involvement in the study
<input checked="" type="checkbox"/>	<input type="checkbox"/> ChIP-seq
<input checked="" type="checkbox"/>	<input type="checkbox"/> Flow cytometry
<input checked="" type="checkbox"/>	<input type="checkbox"/> MRI-based neuroimaging

Animals and other organisms

Policy information about [studies involving animals](#); [ARRIVE guidelines](#) recommended for reporting animal research

Laboratory animals	C57BL/6J, male, the Jackson Laboratory, >8 weeks old; Tg(Rbp4-cre)KL100Gsat, male, the Jackson Laboratory, >8 weeks old; Tg(Thy1-jRGECO1a)GP8.31Dkim/J, male, the Jackson Laboratory, >8 weeks old; B6.Cg-Tg(Thy1-YFP-SLICK A)AGfng/J, male, the Jackson Laboratory, >8 weeks old;
Wild animals	No wild animals were used.
Field-collected samples	No field-collected samples were used.
Ethics oversight	All experimental procedures on our animals were accordance with Guide for the Care and Use of Laboratory Animals and have been approved by Institutional Animal Care and Use Committee at University of California, San Diego.

Note that full information on the approval of the study protocol must also be provided in the manuscript.